THE JOURNAL OF PHYSICAL CHEMISTRY B

Article

pubs.acs.org/JPCB

# Crystalline Structure Changes in Preoriented Metallocene-Based Isotactic Polypropylene upon Annealing

Yan Wang,[†,‡] Jia-Zhuang Xu,[‡] Yan-Hui Chen,[‡] Kai Qiao,[†] Ling Xu,[‡] Xu Ji,[‡] Zhong-Ming Li,*[,‡] and Benjamin S. Hsiao[§]

[†]SINOPEC Fushun Research Institute of Petroleum & Petrochemicals, Liaoning Fushun 113001, China

[‡]College of Polymer Science and Engineering and State Key Laboratory of Polymer Materials Engineering, Sichuan University, Chengdu 610065, China

[§]Department of Chemistry, Stony Brook University, Stony Brook, New York 11794-3400, United States

**ABSTRACT:** Partially melted metallocene-based isotactic polypropylene (m-iPP), which was preoriented with a high degree of molecular orientation and a shish-kebab structure, was annealed at various temperatures and isothermally crystallized at 130 °C. The melting and crystallization process was examined using synchrotron wide-angle X-ray diffraction, small-angle X-ray scattering, and differential scanning calorimetry. For the m-iPP samples annealed at relatively low temperatures, lamellar thickening, lateral growth, and a decrease in the γ-crystal fraction occurred. Because of parallel evolution of α- and γ-crystal growth in the limited crystallizable melt volume, the fraction of γ-crystals was very low. Furthermore, topological constraints in the melt dominate the chain flux in crystal evolution; the chains are consumed by the thickening lamellae and lateral growth, forming α-crystals with parallel chains in the unit cell. For the m-iPP samples isothermally annealed at medium annealing temperatures, the increase in the amount of crystallizable melt caused the γ-crystal fraction to increase. A shish-kebab (α-crystals) structure with high thermal stability and a newly formed macro-unoriented structure coexisted in the final sample. After annealing at high temperatures, at which no crystals survived, γ-crystal formation was greatly favored; this was attributed to the nature of m-iPP molecules and their dynamic behavior at 130 °C. Because of the lack of oriented nuclei, randomly oriented lamellae were formed. On the basis of the structural cooperative changes at different scales, the morphological features at different annealing temperatures were proposed.

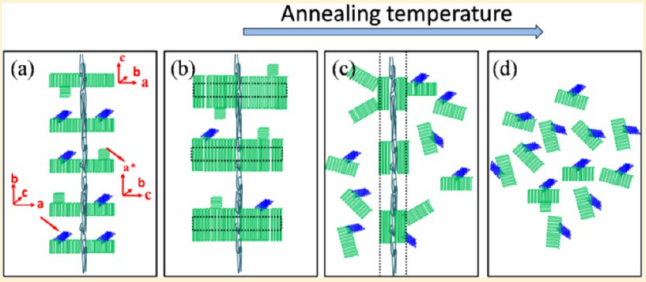


## INTRODUCTION

Practical polymer processing can be used to manipulate the hierarchical structures of semicrystalline polymers at different scales, including polymorphs, molecular orientation, and lamellar structure, to achieve desirable properties.[1−6] However, because of the intrinsic flow and temperature gradients in practical processing, internal stress, warping, and uneven sizes in some parts always impair the mechanical properties. For example, internal stresses in injection-molded parts lead to self-released cracking, and obviously impair the polymer properties.[7] None of the practical processing technologies for semicrystalline polymers can prevent internal stress, and thus post-treatment is particularly important for obtaining satisfactory parts. Annealing, which is one post-treatment method, originally used in metal heat treatments, is an effective way of eliminating internal stress and homogenizing the structure, thus improving the physical properties of the products.[8−11]

The annealing of semicrystalline polymers involves recrystallization and microstructural changes, such as lamellar thickening and polymorphic transformations, and has attracted much attention.[12−18] The annealing of most commercial thermoplastic isotactic polypropylenes (iPP) has been well researched; iPP is more complex than most semicrystalline polymers because of its polymorphs, which include monoclinic α-crystals, trigonal β-crystals, orthorhombic γ-crystals, and a mesomorphic phase. The structures and mechanical properties of iPP in the mesomorphic phase and the α- and β-crystals change significantly on annealing. The mesomorphic structure, which exhibits superior mechanical properties, namely, outstanding ductility and toughness,[19] is gradually transformed to α-monoclinic crystals on annealing at temperatures above 80 °C.[20] When the α-crystals are annealed, the lamellar thickness increases, and the annealed α-iPP has enhanced fracture toughness.[9,21] When β-iPP is annealed at moderate temperatures (120−130 °C), the impact toughness of the iPP is enhanced significantly, without obvious sacrifice of its yield strength; this is mainly attributed to a decrease in the number of chain segments in the amorphous region.[16] γ-Crystals with nonparallel chains are unprecedented in polymeric systems, and γ-iPP shows a higher modulus and higher yield stress compared with α-iPP in plane-strain and uniaxial compression tests.[22,23] However, compared with the considerable amount of work

**Received:** January 24, 2013
**Revised:** May 18, 2013

 © XXXX American Chemical Society  dx.doi.org/10.1021/jp400847p | J. Phys. Chem. B XXXX, XXX, XXX−XXX

Table 1. Metallocene-Based Isotactic Polypropylene Sample Information

| sample | $M_w$ (g/mol)[a] | $M_w/M_n$[a] | $T_m$ (°C)[b] | [mr]%[c] | [rr]%[c] | [mm]%[c] |
|---|---|---|---|---|---|---|
| 562N | 407 000 | 2.25 | 145 | 3.09 | 0.386 | 96.05 |

[a]The molecular weight and $M_w/M_n$ of m-iPP was obtained by gel permeation chromatography (GPC) in 1,2,4-trichlorobenzene at 160 °C. [b]Determined from the peak position of the DSC curves recorded at a heating rate of 10 °C/min. [c]The content of triad stereosequences is obtained from the 13C NMR spectra. The sample was recorded on a Bruker Avance 400 operating at 500 MHz in the Fourier transform mode of 10% w/v polymer solutions in deuterated 1,2,4-trichlorobenzene and benzene at 120 °C.

reported on the effect of annealing on the mesomorphic phase and $\alpha$- and $\beta$-crystals of iPP, the effect of annealing on the formation of $\gamma$-crystals has been less well documented.

The readily available $\gamma$-crystals in metallocene-based isotactic polypropylene (m-iPP) and its copolymers provide an opportunity to understand the thermal properties of the $\gamma$-crystals.[24,25] Recently, we obtained a high content of $\gamma$-crystals in m-iPP parts with high molecular orientation in the outer layer. These m-iPP parts were obtained by the modified injection molding machine—oscillatory shear injection molding (OSIM).[26] The OSIM samples were specially chosen as candidates in the annealing experiments. First, a highly oriented structure is always present in the articles of practical processing. An understanding of the mechanism of annealing in the evolution of the oriented structure could guide the postannealing of iPP articles. Second, highly oriented samples can give more information on structural changes, because orientational relaxation and molecular chain orientation can be used to obtain information on the annealing process.

The present work explored the effects of various annealing temperatures on the polymorphic transformations of preoriented m-iPP, particularly the $\gamma$-crystals, and also the corresponding evolution of microstructures, such as long spacing and lamellar thickness. The structural changes during annealing and subsequent crystallization of the highly oriented molded m-iPP samples were determined using a combination of ex situ differential scanning calorimetry (DSC), in situ two-dimensional wide-angle X-ray diffraction (2D WAXD), and two-dimensional small-angle X-ray scattering (2D SAXS) measurements. The minimum content of $\gamma$-crystals was obtained for all the annealed samples at a medium annealing temperature (147 °C). The structural evolutions of the iPP samples at 147 and 172 °C were analyzed and compared. On the basis of the structural cooperative changes at different scales, a picture of how the morphology of m-iPP changes at different annealing temperatures was proposed.

## EXPERIMENTAL SECTION

**Materials.** Isotactic polypropylene (iPP), polymerized using a metallocene catalyst, was supplied by the Basel Company. Information, such as molecular weight, polydispersity, nominal melting temperature, and content of triad stereosequences, is shown in Table 1.

**Sample Preparation.** The material was first melt-injected into the dumbbell mold of the OSIM machine. A detailed description of OSIM technology has been published previously.[27] Since continuous oscillatory shear was provided at the packing stage of this injection molding cycle, highly oriented bars were obtained. A standard sample with a thickness of 1000 $\mu$m was machined from 300 to 1300 $\mu$m in the transverse direction of the dumbbell bar. This area is referred to as the shear zone and has a high degree of orientation and crystallization, as shown in our previous research.[26]

**Synchrotron X-ray Characterization.** In situ SAXS and WAXD measurements were carried out at the X27C beamline at the National Synchrotron Light Source, Brookhaven National Laboratory. 2D SAXS/WAXD patterns were collected using a MAR CCD X-ray detector (Mar USA, Inc.), which has a resolution of 1024 × 1024 pixels (pixel size = 158 $\mu$m). For the SAXS measurements, the sample-to-detector distance was 1789.7 mm, and the scattering angle was calibrated using silver behenate. For the WAXD measurements, the sample-to-detector distance was 107.6 mm, and the diffraction angle was calibrated using $Al_2O_3$. All the X-ray images (SAXS and WAXD) were corrected for background scattering, air scattering, and beam fluctuations. The 2D WAXD patterns were integrated over the polar angle to convert it to 1D scattering profiles, which gives the intensity change as a function of $q$, $|q| = 4\pi \sin\theta/\lambda$, where $q$ is the absolute value of the scattering vector, $\lambda$ is the wavelength of the X-ray beam (1.371 Å), and $\theta$ is half of the scattering angle. Multipeak Gaussian fitting was used to fit the 1D WAXD profiles, from which the areas of crystalline parts and amorphous halos can be decoupled.[28] The relative crystallinity index ($X_c$) was calculated by

$$X_c = \frac{\sum A_{cryst}}{\sum A_{cryst} + \sum A_{amorp}} \quad (1)$$

where $A_{cryst}$ and $A_{amorp}$ are the fitted areas contributed by the crystalline and amorphous phases, respectively.

The fraction of $\gamma$-crystals was estimated using eq 2, as suggested by Turner-Jones et al.[29]

$$f_\gamma = I_\gamma(117)/[I_\gamma(117) + I_\alpha(130)] \quad (2)$$

where $I_\gamma(117)$ and $I_\alpha(130)$ represent the areas of the corresponding diffraction peaks.

**Experimental Procedures.** An INSTECH hot stage, modified for in situ rheo-X-ray studies, equipped with a precision temperature controller, was used to heat-treat the samples; the accuracy of the temperature control was ±0.1 °C. Briefly, the sample was placed in the gap between two X-ray windows (i.e., a diamond window and a Kapton window) and completely enclosed in the cavity of the measuring cell. The annealing crystallization process was monitored in situ using time-resolved SAXS/WAXS techniques.

Figure 1 shows the crystallization endotherm of the standard state (left) and the scheme for the thermal treatment as a function of time (right). In the left-hand plot, $T_{m_\gamma}$ (137 °C), $T_{m_\alpha}$ (150 °C), and $T_f$ (162 °C) are indicated. The annealing temperatures ($T_n$), $T_n$ = 132 °C (annealing of $\gamma$-crystals), 142 °C (melting of $\gamma$-crystals), 147 °C (melting of $\gamma$-crystals and annealing of $\alpha$-crystals), 154 °C (melting of $\gamma$-crystals and partial melting of $\alpha$-crystals), and 172 °C (above $T_f$), were designated as mPP132, mPP142, mPP147, mPP154, and mPP172.


dx.doi.org/10.1021/jp400847p | J. Phys. Chem. B XXXX, XXX, XXX−XXX

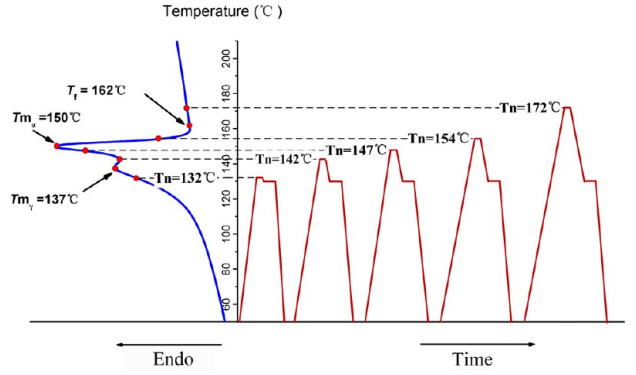


**Figure 1.** DSC thermograms of standard-state m-iPP molded sample at 10 °C/min (left) and heat-treatment protocol of this study.

As shown in Figure 1, the samples were rapidly heated to near the $T_n$ and the heating rate was lowered to 2 °C/min in order to cautiously approach a melting temperature. The melting−annealing temperature was maintained for 10 min. After annealing, the samples were cooled to 130 °C for isothermal crystallization for 10 min and then rapidly cooled to room temperature at 30 °C/min. The entire temperature treatment was an annealing−isothermal−cooling process, and was monitored in a time-resolved manner.

**DSC Measurements.** The DSC measurements were carried out using a TA Instruments Q200 at a scan rate of 10 °C/min, with 5−6 mg of sample under a flowing nitrogen atmosphere, which was calibrated by indium as the standard. In accordance with the samples of 2D WAXD and SAXS measurements, the samples for DSC measurement were the ones after cooling to room temperature.

## RESULTS

**Crystalline Structures of Original Preoriented m-iPP Sample.** Figure 2a,c shows the 2D WAXD and 2D SAXS patterns of the original preoriented sample obtained from the OSIM bar. The 2D WAXD and 2D SAXS patterns both show strong azimuthal dependence, indicating high crystalline orientation, as expected. The 1D WAXD curve in Figure 2b shows the coexistence of $\alpha$- and $\gamma$-crystals; the fraction of $\gamma$-crystals ($f_\gamma$) and the crystallinity were calculated to be 0.71 and 0.471, respectively. The 1D SAXS curve in Figure 2d is typical for a semicrystalline polymer; the long spacing, obtained using $L = 2\pi/q$, is 13.5 nm. The degree of lamellar orientation, $F$ = 0.85, was also obtained, and indicated a high degree of molecular chains in the original preoriented sample.

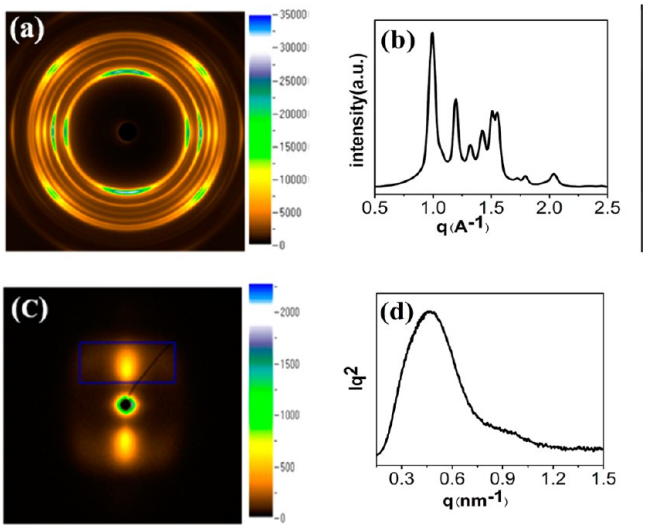


**Figure 2.** Structure of original preoriented m-iPP sample: (a) 2D WAXD pattern of original sample; (b) 1D WAXD intensity profile obtained from circularly integrated intensities in (a); (c) 2D SAXS pattern of original sample; and (d) 1D SAXS intensity profile obtained from circularly integrated intensities in (c).

**Crystalline Structures at Annealing Temperatures.** The microstructures of the original preoriented sample were determined using WAXD and SAXS at different annealing temperatures ($T_n$), as shown in Figure 3. The diffraction rings of the original preoriented WAXD patterns weaken with increasing $T_n$ because the crystallites gradually melt. For the SAXS patterns, scattering of the ordered structure, as well as anisotropic behavior, can be observed in all samples except for the one annealed at the highest temperature, 172 °C. No lamellae remain at 172 °C because the crystals have completely melted.

Quantitative WAXD and SAXS data obtained at different $T_n$ values are shown in Figure 4. The crystallinity gradually decreases from 0.35 to 0.23 (Figure 4b), and the long spacing increases from 20 to 23.3 nm (Figure 4d), with increasing $T_n$ up to 147 °C. At an annealing temperature of 154 °C, some $\alpha$-crystals are still preserved, but there are no traces of $\gamma$-crystals. The crystallinity further decreases to 0.15 (Figure 4b), and the long spacing slightly increases to 23.8 (Figure 4d), compared with mPP147. This suggests that the decrease in the crystallinity did not damage the lamellar skeleton. Moreover, a high degree of lamellar orientation is preserved (Figure 4f), indicating that the residual skeleton of the lamellae at 154 °C was preserved.[30] When the annealing temperature is 172 °C, the ordered structure completely disappears, as shown by the WAXD and SAXS patterns (Figure 3), associated with the collapse of all ordered structures at the highest $T_n$, that is, 172 °C.

**Crystalline Structure Evolution on Annealing.** The evolution of the crystal and lamellar structures during the entire annealing−isothermal−cooling process was monitored in situ for all the samples. The mPP147 and mPP172 samples, which represent the medium annealing temperature sample and the highest annealing temperature sample, respectively, are taken as examples for developing an in-depth understanding of the structural changes on recrystallization.

The structural evolution of mPP147 during the annealing−isothermal−cooling process is illustrated in Figure 5. As the temperature rises to 147 °C at 10 °C/min, the $\gamma$-crystals are almost melted ($X_\gamma$ = 0.03), whereas a large number of $\alpha$-crystals are still intact; that is, $X_\alpha$ = 0.20 (Figure 4b). If the upper limit of crystallinity, which is about 0.47 (as estimated from the original preoriented sample), excludes the residual crystallinity $X_\alpha$ = 0.20, a melt weight fraction for crystallization of about only 0.24 at 147 °C is obtained. When the sample is isothermally crystallized at 130 °C, $X_\gamma$ and $X_\alpha$ rapidly increase from 0.03 and 0.20 to 0.17 and 0.29, respectively (Figure 5a,b). When the sample is cooled, the crystallinity is almost unchanged. The 1D SAXS data (Figure 5c) were used to determine the evolution of the crystalline lamellar long spacing (Figure 5d). The results show that the long spacing shows only a slight decrease from 14.8 to 13.8 nm during annealing, and basically remains unchanged during cooling.


dx.doi.org/10.1021/jp400847p | J. Phys. Chem. B XXXX, XXX, XXX−XXX

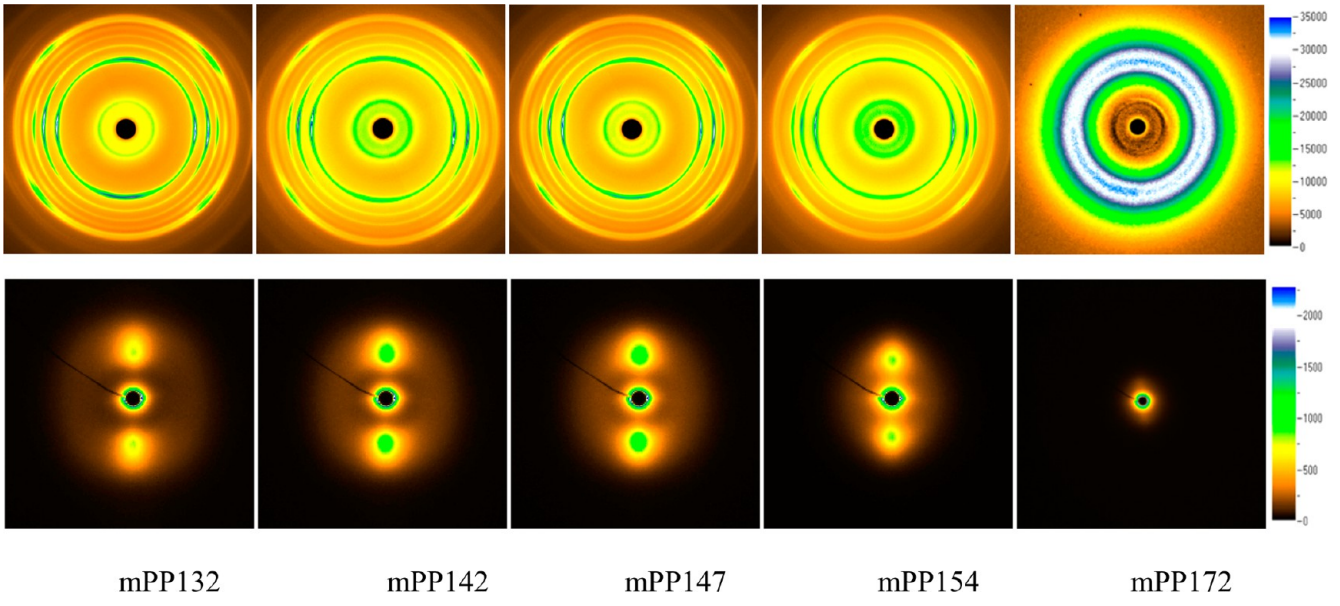


**Figure 3.** 2D WAXD (top) and 2D SAXS (bottom) patterns, obtained immediately after annealing at different temperatures, of molded m-iPP samples. The flow direction is vertical. The images were corrected by air scattering.

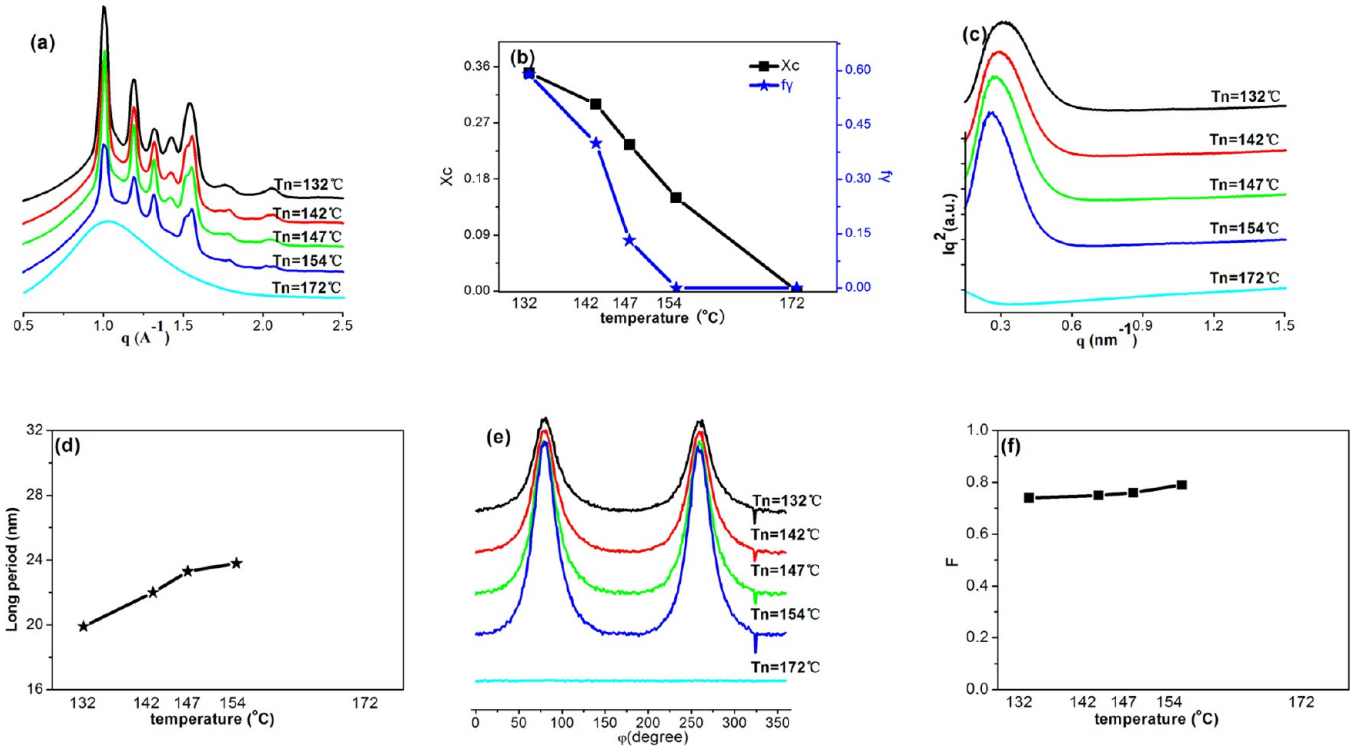


**Figure 4.** WAXD and SAXS data immediately after annealing at different temperatures: (a) 1D WAXD; (b) crystallinity, $X_c$, and fraction of $\gamma$-crystals, $f_\gamma$; (c) 1D SAXS; (d) long spacing, $L$; (e) azimuthal scan from 1D SAXS; and (f) degree of orientation, $F$.

The structural evolution of mPP172 during the entire annealing−isothermal−cooling process is shown in Figure 6. In Figure 6b, on cooling to $T_c$, after an induction period of 4 min, $\alpha$- and $\gamma$-crystals appear simultaneously. The crystallinity of the $\alpha$- and $\gamma$-crystals increases with time. Saturation of the $\alpha$-crystals ($X_\alpha$ = 0.1) appears 1 min after the induction period. After 35 min of isothermal crystallization, $X_\gamma$ finally increases to saturation ($X_\gamma$ = 0.22). The results suggest that $\gamma$-crystal formation under isothermal crystallization at 130 °C is favored. This could be attributed to the nature of the m-iPP molecules and their dynamic behavior at 130 °C; this is in line with our previous research.[31] It is interesting that, on cooling, $X_\gamma$ dramatically increases to 0.37, indicating that secondary crystallization facilitates the deposition of $\gamma$-crystal layers.[32] On the basis of the SAXS data, the evolution of the lamellar structure is summarized in Figure 6c. As crystallization proceeds, the long spacing appears after 4 min during isothermal crystallization, changing from 28 to 14 nm (Figure 6d).


dx.doi.org/10.1021/jp400847p | J. Phys. Chem. B XXXX, XXX, XXX−XXX

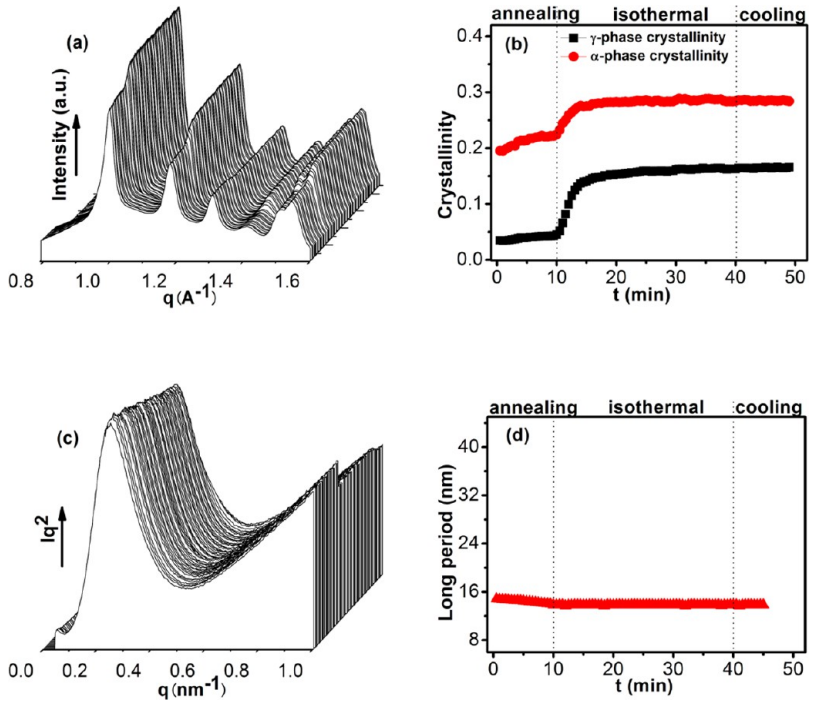


**Figure 5.** Time evolution of 1D WAXD profiles (a); evolution of $\alpha$- and $\gamma$-crystals (b); time evolution of 1D SAXS profiles (c); and evolution of long spacing (d) during annealing, isothermal crystallization, and cooling period for mPP147.

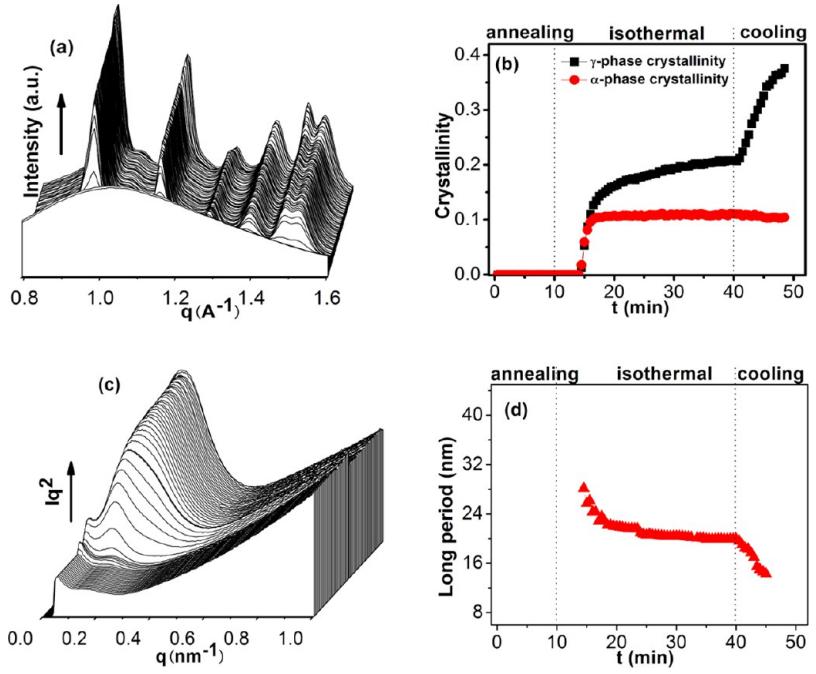


**Figure 6.** Time evolution of 1D WAXD profiles (a); evolution of $\alpha$- and $\gamma$-crystals (b); time evolution of 1D SAXS profiles (c); and evolution of long spacing (d) during annealing, isothermal crystallization, and cooling period for mPP172.

**Crystalline Structures at Room Temperature after Annealing.** The crystal structures of all the as-annealed samples at room temperature were investigated. 2D WAXD patterns are shown in Figure 7. As the $T_n$ increases, the crystalline orientation gradually fades, and the anisotropic arclike patterns change to isotropic ones. Figure 7a shows the integrated WAXD profiles, and the corresponding crystallinity and fraction of $\gamma$-crystals ($f_\gamma$) are summarized in Table 2. The crystallinity ($X_c$) does not rely on the $T_n$, whereas $f_\gamma$ dramatically decreases from 0.71 for the original sample to 0.39 for mPP147, but subsequently increases to 0.8 for mPP172. It is interesting to note that $f_\gamma$ changes nonmonotonically with increasing $T_n$. Since $\gamma$-crystals are favored at higher temperatures,[33] it is unexpected that the samples annealed at higher $T_n$ values (e.g., $T_n$ = 147 °C) contain fewer $\gamma$-crystals than those annealed at lower $T_n$. The widely accepted mechanism that is thermodynamically favored for $\gamma$-crystal


dx.doi.org/10.1021/jp400847p | J. Phys. Chem. B XXXX, XXX, XXX−XXX

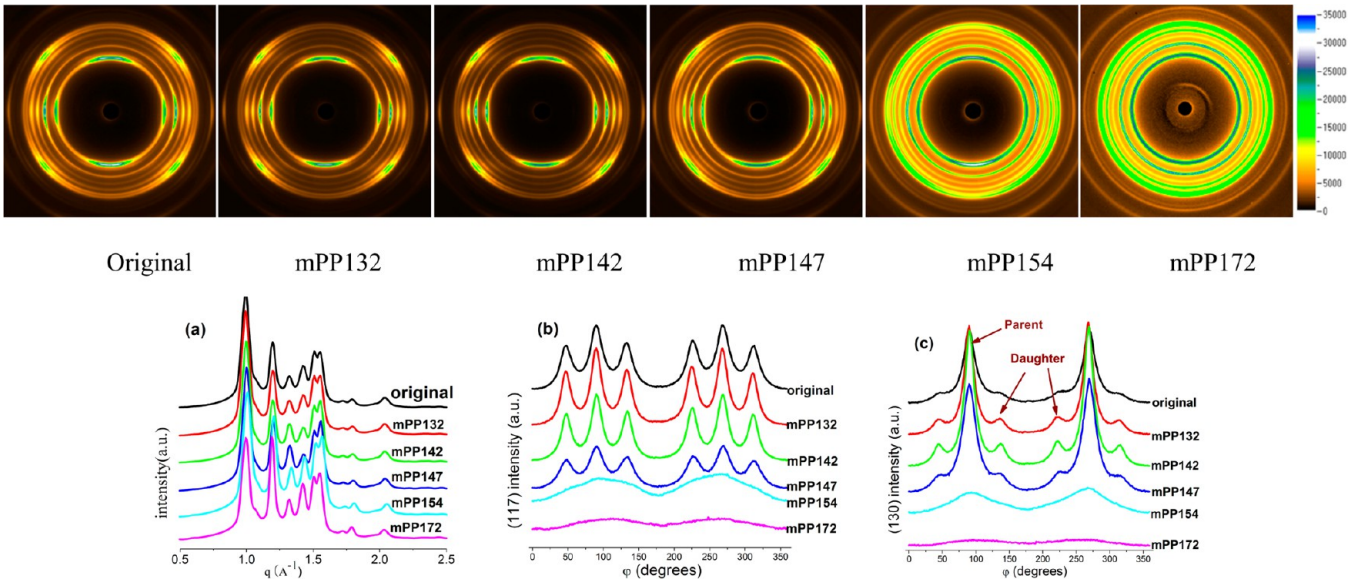


**Figure 7.** 2D WAXD patterns (top). Plots of integrated WAXD intensity as a function of $q$ ($A^{-1}$) (a); and azimuthal profiles $I(\varphi)$ of $(117)_\gamma$ (b) and $(130)_\alpha$ (c) reflections as a function of azimuthal angle $\varphi$, taken at room temperature after annealing at different temperatures. For 2D WAXD patterns, the flow direction is vertical. The patterns were corrected by air scattering.

**Table 2. Crystallinity ($X_c$) and Fraction of $\gamma$-Crystals ($f_\gamma$) Estimated from 1D WAXD, and Parent/Daughter Ratio [$R$] Estimated from Azimuthal Profiles of $(130)_\alpha$ at Room Temperature**

| | original | mPP132 | mPP142 | mPP147 | mPP154 | mPP172 |
|---|---|---|---|---|---|---|
| $X_c$ | 0.471 | 0.471 | 0.471 | 0.471 | 0.471 | 0.470 |
| $f_\gamma$ | 0.71 | 0.61 | 0.46 | 0.39 | 0.61 | 0.80 |
| $R$ | 7.67 | 5.64 | 4.98 | 4.34 | | |

formation, therefore, does not seem to apply to the annealed samples, so another mechanism must be involved.

Orientational relaxation accompanied by chain relaxation would occur under annealing, which inevitably affects the crystalline forms.[34] The crystalline orientations of the as-annealed samples were, therefore, further examined to investigate the relationship between the crystalline forms and orientations of the chains and lamellae. The azimuthal scans of $(117)_\gamma$ are compiled in Figure 7b. The original three-peak azimuthal profile of the $\gamma$-crystals indicates a parallel-chain axis orientation of the $\gamma$-crystals,[35] which represents a preferred orientation with one-half of the chain axes parallel to the stretching direction and the second half of the chains directed at an angle of ≈81° with respect to the fiber axis. This oriented structure is consistent with the orientations of the chains in samples prepared using the OSIM technique in a previous study,[26] as well as with those on the surface of pitch-based

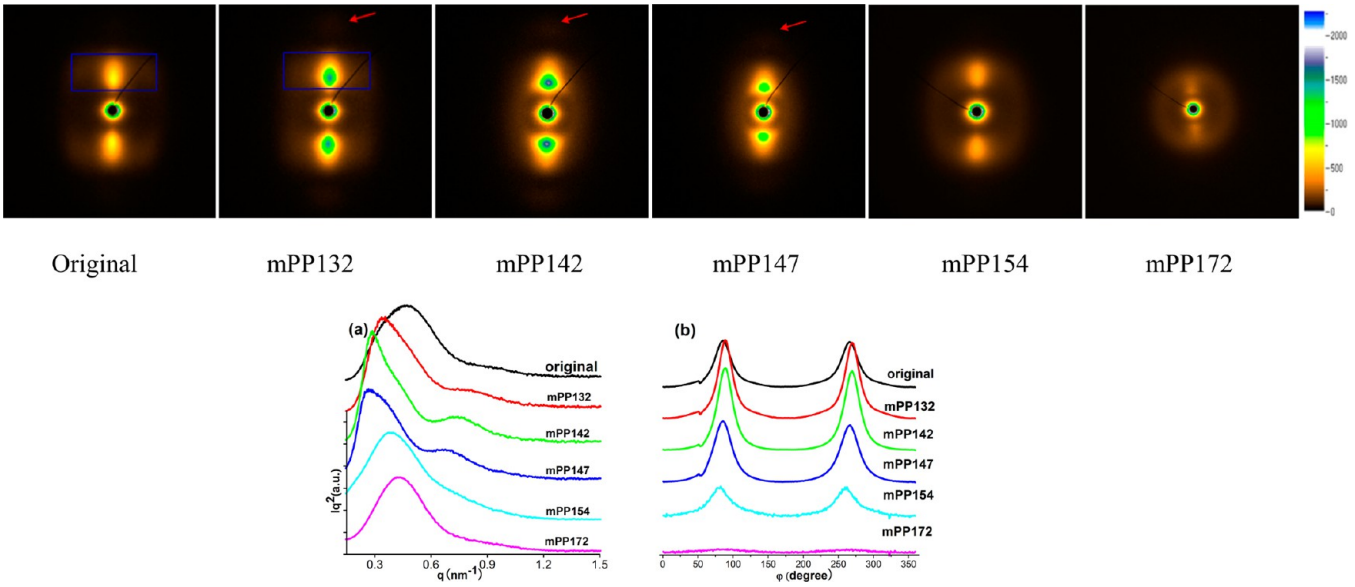


**Figure 8.** 2D SAXS patterns (top). Lorentz-corrected 1D SAXS intensity profiles (a); and azimuthal scans in SAXS patterns (b), taken at room temperature after annealing at different temperatures of molded m-iPP samples. The flow direction is vertical. The images were corrected by air scattering.


dx.doi.org/10.1021/jp400847p | J. Phys. Chem. B XXXX, XXX, XXX−XXX

carbon or Kevlar fiber-reinforced iPP composite fibers.[36,37] With increasing $T_n$, the three-peak azimuthal profile becomes a single-peak profile for mPP154, and the orientation profile is completely absent for mPP172. Cao et al.[38] reported that a small-angle change of the stem orientation of the $\alpha$-form has a profound effect on the formation of the $\gamma$-form in iPP as a result of the molecular epitaxy of the $\gamma$-crystals on the $\alpha$-crystals. To further elucidate the epitaxy between the $\gamma$- and $\alpha$-crystals, analysis of the orientation of the $\alpha$-crystals is shown in Figure 7c.

Three-peak azimuthal profiles also appear for the $(130)_\alpha$ reflection, which is similar to the three-peak $(117)_\gamma$ reflection. This is attributed to the existence of parent lamellae and daughter lamellae. The ratio of parent lamellae to daughter lamellae, $[R]$, for the $(130)_\alpha$ reflection can be estimated using the method suggested by Fujiyama, as follows[39]

$$[R] = \frac{2P}{D_1 + D_2} \quad (3)$$

where $P$ is the area around the azimuthal angle of 90°, and $D_1$ and $D_2$ represent the areas around 45° and 135°, respectively, after subtraction of the baseline area. Using the above equation, the original parent/daughter ratio, $[R]$, is found to be 7.67. $[R]$ is smallest (4.34) for mPP147, which coincides with the smallest $f_\gamma$ (0.39). This result can be explained as follows. The reduction in $[R]$ implies a relatively low content of parent lamellae, providing fewer nucleating locations, and space competition between daughter lamellae and $\gamma$-crystals causes the lowest $f_\gamma$ in the final sample.[26] It is worth noting that relatively flat azimuthal patterns (from which $[R]$ cannot be obtained) are formed for mPP154 and mPP172, indicating that an approximately random orientation of the $\alpha$-crystals causes randomly oriented $\gamma$-crystals.

The lamellar structures of the as-annealed samples were examined using 2D SAXS, and the patterns are shown in Figure 8. For the original sample, in addition to a pair of visible and narrow meridional maxima, an obscure and wide four-point pattern, marked by a rectangle, is also seen. This is attributed to the existence of two preferred orientations,[40] which would contain the periodic arrangement of the parent lamellae and preferred orientations of the daughter lamellae and $\gamma$-crystals. The four-point pattern is absent at slightly higher $T_n$ (142 °C). For as-annealed mPP132, mPP142, and mPP147, additional dim meridional scattering appears (marked by arrows), which represents second-order scattering. This characteristic is much easier to recognize in the 1D SAXS curves.

The Lorentz-corrected 1D SAXS profiles are shown in Figure 8a. For as-annealed mPP132, mPP142, and mPP147, the 1D SAXS curves show a relatively sharp primary peak with a secondary peak of much lower intensity at a higher scattering vector value, indicating that the periodicity of the lamellae becomes higher. In addition, a sharper and narrower scattering feature also suggests lateral growth of crystallites and increasing order along the orientation direction.[40,41] The long spacing ($L$) is estimated from the primary peak position, and the corresponding lamellar thickness ($L_c$) is generally calculated by multiplying the long spacing by the crystalline fraction ($X_c$). The calculated values are listed in Table 3. The long spacing first increases and then decreases with increasing $T_n$, exhibiting a maximum for the mPP147 sample. Obviously, the lamellar thickness follows the same trend as that of the long spacing because of the almost constant crystallinity. Interestingly, the highest lamellar thickness, about 11.2 nm, corresponds to the lowest $f_\gamma$ (0.39) in Tables 2 and 3. This may be attributed to the fact that lamellar thickening is not favorable for $\gamma$-crystals; this will be discussed later.

**Table 3. Long Spacing ($L$), Lamellar Thickness ($L_c$), and Degree of Orientation ($F$) at Room Temperature after Annealing at Different Temperatures, Estimated from SAXS**

| | original | mPP132 | mPP142 | mPP147 | mPP154 | mPP172 |
|---|---|---|---|---|---|---|
| $L$ (nm) | 13.5 | 17.6 | 21.8 | 23.8 | 15.4 | 13.8 |
| $L_c$ (nm) | 6.4 | 8.3 | 10.3 | 11.2 | 7.3 | 6.5 |
| $F$ | 0.85 | 0.89 | 0.89 | 0.87 | 0.15 | 0 |

Figure 8b shows the azimuthal profiles of the 2D SAXS patterns of the as-annealed samples. The quantitative Hermans orientation is used to evaluate the lamellar orientation, and the values are listed in Table 3. The lamellar orientation increases slightly (Table 3) for as-annealed mPP132, mPP142, and mPP147 as a result of formation of more perfect crystals, and obviously decreases for as-annealed mPP154 and mPP172 because of melting of the highly oriented $\alpha$-crystals.

DSC was performed to reveal the microstructural changes after annealing. Figure 9 shows the DSC thermograms of as-annealed samples with different annealing temperatures. Two typical melting peaks are the clearest feature in all the samples at a heating rate of 10 °C/min; these can be attributed to the coexistence of $\gamma$- and $\alpha$-crystals.[33] The broad low-temperature endotherm (120−145 °C) represents the melting of $\gamma$-crystals, and the narrow endotherm (within 5 °C) at around 149 °C at relatively high temperature can be attributed to melting of the more ordered $\alpha$-crystals. The melting peak temperature of the $\alpha$-crystals ($T_{m_\alpha}$) clearly shifts toward higher temperature with increasing $T_n$, except in the case of the highest annealing temperature, 172 °C. Compared with the original sample ($T_{m_\alpha}$ = 149.5 °C), $T_{m_\alpha}$ for as-annealed mPP132, mPP142, and mPP147 increased by 1, 4, and 7 °C ($T_{m_\alpha}$ = 150.5, 153.5, and 156.5 °C), respectively. According to the Gibbs−Thomson equation, the maximum melting temperature is directly proportional to the maximum lamellar thickness. An increase in the melting temperature, therefore, results in thickening of the lamellae, which further supports the SAXS results. For the mPP154 sample, in addition to two typical melting peaks of the crystals, an unexpected small additional melting peak appears at 158 °C. For mPP172, an obvious decrease in the melting temperature of the $\alpha$-crystals is observed, which could be attributed to total collapse of the preoriented crystals, hence the lack of lamellar thickening.

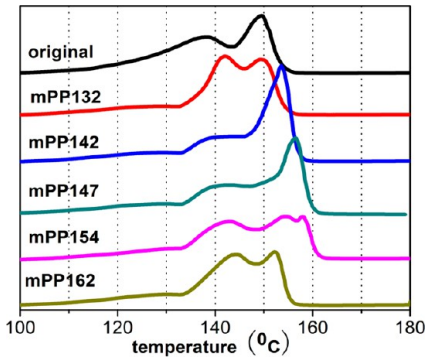


**Figure 9.** DSC curves of samples at a heating rate of 10 °C/min.


dx.doi.org/10.1021/jp400847p | J. Phys. Chem. B XXXX, XXX, XXX−XXX

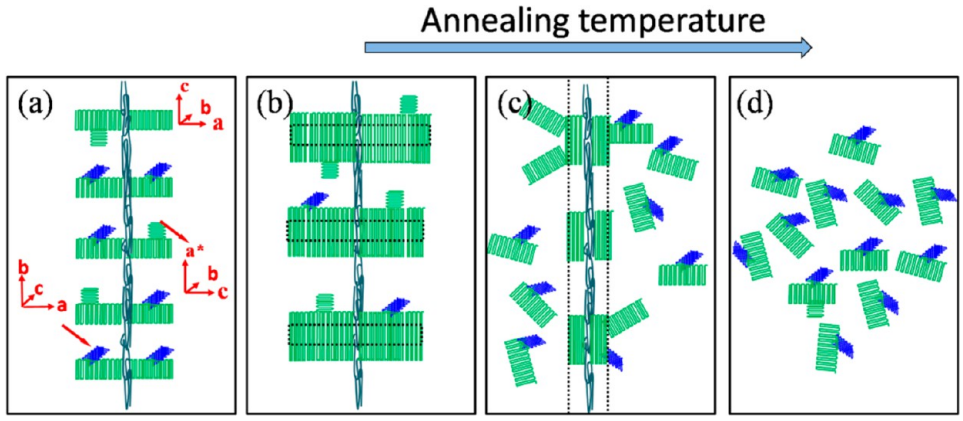


**Figure 10.** Schematic diagram of morphological evolution after annealing at different temperatures. Green represents the parent lamellae and daughter lamellae, and blue represents γ-lamellae. The structures on the dotted line represent the structures at the annealing temperature.

## DISCUSSION

The above results indicate interesting structural changes during the annealing−isothermal−cooling process, enabling the crystalline forms, lamellar structures, and crystalline and lamellar orientations to be envisaged. For the samples after annealing at relatively low $T_n$ (lower than 147 °C), lamellar thickening and lateral growth, accompanied by a decrease in the fraction of γ-crystals, occur. In contrast, when $T_n$ is greater than 147 °C, the fraction of γ-crystals increases with increasing annealing temperature, and the lamellae become thinner. However, it is not clear how polymorphic transformation accompanies lamellar thickening and changes in structural orientation during the annealing process. On the basis of the above, apparently diverse, facts, a simple schematic diagram is shown in Figure 10 to help fully understand the polymorphic transformation and microstructural evolution.

For the original sample, a lamella-branched shish-kebab structure, which is characterized by an epitaxial arrangement between the γ-phase and the shish-kebab α-phase, is proposed, as shown in Figure 10a. As stated in our previous work,[26] the parent lamellae have their *c* axes preferentially aligned along the flow direction, the daughter lamellae have their *a** axes parallel to the flow direction, and the *b* axis of the γ-crystals is tilted by ±40.7° to the connected α-parent lamellae.

Compared with the original sample, decreases in the amounts of γ-crystals and increases in the lamellar thickness are observed in the samples annealed below 147 °C. A large amount of residual α-crystals ($X_\alpha$ = 0.2) is obtained at 147 °C. γ-Crystals can only be obtained in the subsequent parallel evolution of α- and γ-crystals during crystallization, resulting in limited numbers of γ-crystals in the final sample. This explanation is certainly applicable to mPP132 and mPP142. However, the larger amounts of residual γ-crystals in these two systems than in mPP147 at $T_n$ result in larger contents of γ-crystals in the final samples. The WAXD and SAXS data suggest that no obvious new lamellae are formed between adjacent lamellae for the sample annealed below 147 °C, and the lamellar thickening could account for crystallization. For the sample annealed below 147 °C, it is reasonable to propose the diagram shown in Figure 10b. The lamellae on the dotted line represent the residual structures at $T_n$, and the entire diagram shows all the crystallites after recrystallization. The lamellar thickening of α-crystals and decreased γ-crystal fraction are explained by this diagram. Furthermore, a high degree of orientation is naturally obtained.

As the annealing temperature rises to 154 °C, the situation is quite different from that for samples below 147 °C. As proposed in Figure 10c, the annealing treatment destroys the partial unstable kebab lamellae, but the core of the lamellae (the shish and some kebabs of α-crystals) with high thermal stability still survives, as shown by the dotted line. When crystallization proceeds, the newly formed lamellae on the residual lamellae and/or the newly formed randomly oriented lamellae between distant oriented crystals appear. The decrease in the orientation and the long spacing can be explained. The crystallization evolution also features parallel evolution of α- and γ-crystals; the increase in the amount of crystallizable melt at relatively high annealing temperatures causes an increase in the fraction of γ-crystals ($f_\gamma$ = 0.61); that is, the content of γ-crystals in the final mPP154 increases. Similarly, because of the complete melting of the original sample and the subsequent parallel evolution of α- and γ-crystals, the final γ-crystal lamellae in the mPP172 sample are dominant ($f_\gamma$ = 0.8). A macro-unoriented structure is also formed, that is, randomly oriented lamellae, as illustrated in Figure 10d.

In addition to dynamic factors, that is, parallel evolution of α- and γ-crystals, with the lowest crystallizable volumes at the annealing temperature causing the lowest content of γ-crystals in mPP147, there is another possible factor causing suppression of γ-crystals in the mPP147 sample, from the perspective of rigid amorphous chains.[42] We define two parameters, $f_{\Delta\gamma}$ and $f_{\Delta\alpha}$, which represent the regeneration ability of γ- and α-crystals, respectively, in the residual melt, as follows: $f_{\Delta\gamma} = \Delta\gamma/(\Delta\gamma + \Delta\alpha)$ and $f_{\Delta\alpha} = \Delta\alpha/(\Delta\gamma + \Delta\alpha)$, where $\Delta\alpha$ and $\Delta\gamma$, respectively, are the values of the increased crystallinity of the α- and γ-crystals during isothermal crystallization. The values for mPP147 and mPP172 are given for a direct comparison. For mPP147, $f_{\Delta\gamma}$ = 0.6 and $f_{\Delta\alpha}$ = 0.4; for mPP172, $f_{\Delta\gamma}$ = 0.68 and $f_{\Delta\alpha}$ = 0.22. These results confirm that the ability of the mPP147 melt to reform γ-crystals is lower than that of mPP172. It is conceivable that, in the mPP147 sample, there is a certain fraction of chains across phase boundaries constrained by their attachment to the crystalline ordered structure at the annealing temperature. In fact, the assignment of constrained amorphous chains, also known as rigid amorphous chains, has been adopted in many reports in the literature.[43−46] These chains cannot relax freely, and remain oriented at lower annealing temperatures, which has an impact on the final crystal structure. This can be understood as follows. The chains in the melt between two α-crystal lamellae always emerge from these


dx.doi.org/10.1021/jp400847p | J. Phys. Chem. B XXXX, XXX, XXX−XXX

lamellae as a result of chain entanglement; at least some of the chains in the melt are constrained by the nearest or the next nearest neighbor crystalline lamellae from the point at which they emanate. These topological constraints in the melt lead to the conclusion that the chains cannot fold significantly when evolving crystals.[33] However, the chain flux can be dissipated in another way. Crystallization can proceed by lamellar thickening and lateral growth, forming $\alpha$-crystals. Only some of the individual chain units can, therefore, participate in producing $\gamma$-crystals, leading to the small fractions of $\gamma$-crystals formed in the final sample, as in the case of mPP147. This view is indirectly supported by the work of Dai et al., who obtained the lowest fraction of $\gamma$-crystals at medium temperature when annealing unoriented samples.[25] In contrast, in the absence of local constraints from rigid amorphous chains, for mPP172, the dynamic factor and the nature of the molecular chains facilitate formation of $\gamma$-crystals during isothermal processing, and further enhance $\gamma$-crystal formation by secondary crystallization during cooling.

## CONCLUSIONS

The crystallization behavior of m-iPP for a series of annealing temperatures was studied by in situ 2D WAXD and 2D SAXS, and ex situ DSC. The results provide evidence of distinct changes in the crystalline forms and lamellar thicknesses, and unique orientation structures during crystallization. On the basis of the cooperative structural changes at different scales, a schematic diagram representing the morphological characteristics at different annealing temperatures is also proposed. For samples after annealing at relatively low temperatures (lower than 147 °C), lamellar thickening and lateral growth, accompanied by decreased fractions of $\gamma$-crystals, are observed. As a result of parallel evolution of $\alpha$- and $\gamma$-crystal growth in the limited crystallizable melt volume, the final fraction of $\gamma$-crystals is very low. Furthermore, topological constraints in the melt dominate the chain flux in crystal evolution; the chains are consumed by the thickening lamellae and lateral growth, forming $\alpha$-crystals with parallel chains in the unit cell. For samples after annealing at a medium temperature (154 °C), the increase in the amount of crystallizable melt causes the content of $\gamma$-crystals to increase. A shish-kebab ($\alpha$-crystals) structure with high thermal stability and newly formed macro-unoriented structures coexist in the final sample. After annealing at a high temperature (172 °C), in which there are no crystals ($\alpha$- or $\gamma$-crystal) at the annealing temperature, $\gamma$-crystal formation under isothermal crystallization at 130 °C is favored; this is attributed to the nature of the m-iPP molecules and the dynamic behavior at 130 °C. During the isothermal stage, saturation of the $\alpha$-crystals ($X_\alpha = 0.1$) appears at 1 min after the induction period; $X_\gamma$ gradually increases to $X_\gamma = 0.22$ until the end of isothermal crystallization. On cooling, $X_\gamma$ increases significantly to 0.37, indicating that secondary crystallization facilitates $\gamma$-crystal formation. As a result of a lack of oriented nuclei, randomly oriented lamellae are formed. This research shows how the morphology of m-iPP changes at different annealing temperatures. The results show how molded samples respond to annealing temperature, and could be useful as a guide in postannealing of molded iPP articles.

## AUTHOR INFORMATION

### Corresponding Author

*Tel: +86-28-8540-6866. Fax: +86-28-8540-6866. E-mail: zmli@scu.edu.cn.

### Notes

The authors declare no competing financial interest.

## ACKNOWLEDGMENTS

The authors are indebted to Dr. Lixia Rong from the National Synchrotron Light Source, Brookhaven National Laboratory (USA), and Prof. Guoqiang Pan from National Synchrotron Radiation Laboratory, Hefei, China, for their help with in situ synchrotron X-ray scattering measurements. The Chinese team thanks the National Outstanding Youth Foundation of China (Grant No. 50925311), the Foundation for Innovative Research Groups of the National Natural Science Foundation of China (Grant No. 51121001), and the National Natural Science of China (Grant No. 51273131) for financial assistance, and the U.S. team thanks the National Science Foundation of the U.S. (DMR-0906512) for financial support.

## REFERENCES

(1) Kalay, G.; Bevis, M. J. Processing and Physical Property Relationships in Injection Molded Isotactic Polypropylene. 1. Mechanical Properties. *J. Polym. Sci., Part B: Polym. Phys.* **1997**, *35*, 241−263.

(2) Kalay, G.; Bevis, M. J. Processing and Physical Property Relationships in Injection-Molded Isotactic Polypropylene. 2. Morphology and Crystallinity. *J. Polym. Sci., Part B: Polym. Phys.* **1997**, *35*, 265−291.

(3) Cao, W.; Wang, K.; Zhang, Q.; Du, R.; Fu, Q. The Hierarchy Structure and Orientation of High Density Polyethylene Obtained via Dynamic Packing Injection Molding. *Polymer* **2006**, *47*, 6857−6867.

(4) Zhu, P. W.; Edward, G. Orientational Distribution of Parent−Daughter Structure of Isotactic Polypropylene: A Study Using Simultaneous Synchrotron WAXS and SAXS. *J. Mater. Sci.* **2008**, *43*, 6459−6467.

(5) Zhong, G. J.; Li, Z. M.; Li, L. B.; Shen, K. Z. Crystallization of Oriented Isotactic Polypropylene (iPP) in the Presence of in Situ Poly(ethylene terephthalate) (PET) Microfibrils. *Polymer* **2008**, *49*, 4271−4278.

(6) Chen, Y. H.; Zhong, G. J.; Wang, Y.; Li, Z. M.; Li, L. B. Unusual Tuning of Mechanical Properties of Isotactic Polypropylene Using Counteraction of Shear Flow and $\beta$-Nucleating Agent on $\beta$-Form Nucleation. *Macromolecules* **2009**, *42*, 4343−4348.

(7) Postawa, P.; Kwiatkowski, D. Residual Stress Distribution in Injection Molded Parts. *J. Achiev. Mater. Manuf. Eng.* **2006**, *18*, 171−174.

(8) Choudhury, R. P.; Lee, J. S.; Kriegel, R. M.; Koros, W. J.; Beckham, H. W. Chain Dynamics in Antiplasticized and Annealed Poly(ethylene terephthalate) Determined by Solid-State NMR and Correlated with Enhanced Barrier Properties. *Macromolecules* **2012**, *45*, 879−887.

(9) Ferrer-Balas, D.; Maspoch, M. L.; Martinez, A. B.; Santana, O. O. Influence of Annealing on the Microstructural, Tensile and Fracture Properties of Polypropylene Films. *Polymer* **2001**, *42*, 1697−1705.

(10) Na, B.; Tian, N. N.; Lv, R. H.; Zou, S. F.; Xu, W. F.; Fu, Q. Annealing-Induced Oriented Crystallization and Its Influence on the Mechanical Responses in the Melt-Spun Monofilament of Poly(l-lactide). *Macromolecules* **2010**, *43*, 1156−1158.

(11) Liu, Y.; Cui, L.; Guan, F.; Gao, Y.; Hedin, N. E.; Zhu, L.; Fong, H. Crystalline Morphology and Polymorphic Phase Transitions in Electrospun Nylon-6 Nanofibers. *Macromolecules* **2007**, *40*, 6283−6290.

(12) Maiti, P.; Hikosaka, M.; Yamada, K.; Toda, A.; Gu, F. Lamellar Thickening in Isotactic Polypropylene with High Tacticity Crystallized at High Temperature. *Macromolecules* **2000**, *33*, 9069−9075.

(13) Marand, H.; Huang, Z. Isothermal Lamellar Thickening in Linear Polyethylene: Correlation between the Evolution of the Degree of Crystallinity and the Melting Temperature. *Macromolecules* **2004**, *37*, 6492−6497.

(14) Mezghani, K.; Anderson Campbell, R.; Phillips, P. J. Lamellar Thickening and the Equilibrium Melting Point of Polypropylene. *Macromolecules* **1994**, *27*, 997−1002.
(15) Rochette, C. N.; Rosenfeldt, S.; Henzler, K.; Polzer, F.; Ballauff, M.; Tong, Q.; Mecking, S.; Drechsler, M.; Narayanan, T.; Harnau, L. Annealing of Single Lamella Nanoparticles of Polyethylene. *Macromolecules* **2011**, *44*, 4845−4851.
(16) Bai, H.; Wang, Y.; Zhang, Z.; Han, L.; Li, Y.; Liu, L.; Zhou, Z.; Men, Y. Influence of Annealing on Microstructure and Mechanical Properties of Isotactic Polypropylene with β-Phase Nucleating Agent. *Macromolecules* **2009**, *42*, 6647−6655.
(17) Bai, H. W.; Deng, H.; Zhang, Q.; Wang, K.; Fu, Q.; Zhang, Z. J.; Men, Y. F. Effect of Annealing on the Microstructure and Mechanical Properties of Polypropylene with Oriented Shish-Kebab Structure. *Polym. Int.* **2012**, *61*, 252−258.
(18) Zhao, J. C.; Wang, Z. G.; Niu, Y. H.; Hsiao, B. S.; Piccarolo, S. Phase Transitions in Prequenched Mesomorphic Isotactic Polypropylene during Heating and Annealing Processes As Revealed by Simultaneous Synchrotron SAXS and WAXD Technique. *J. Phys. Chem. B* **2012**, *116*, 147−153.
(19) Zia, Q.; Radusch, H. J.; Androsch, R. Deformation Behavior of Isotactic Polypropylene Crystallized via a Mesophase. *Polym. Bull.* **2009**, *63*, 755−771.
(20) Wang, Z. G.; Hsiao, B. S.; Srinivas, S.; Brown, G. M.; Tsou, A. H.; Cheng, S. Z. D.; Stein, R. S. Phase Transformation in Quenched Mesomorphic Isotactic Polypropylene. *Polymer* **2001**, *42*, 7561−7566.
(21) Frontini, P. M.; Fave, A. The Effect of Annealing Temperature on the Fracture Performance of Isotactic Polypropylene. *J. Mater. Sci.* **1995**, *30*, 2446−2454.
(22) Lezak, E.; Bartczak, Z.; Galeski, A. Plastic Deformation of the γ Phase in Isotactic Polypropylene in Plane-Strain Compression. *Macromolecules* **2006**, *39*, 4811−4819.
(23) Lezak, E.; Bartczak, Z. Plastic Deformation of the γ Phase Isotactic Polypropylene in Plane−Strain Compression at Elevated Temperatures. *Macromolecules* **2007**, *40*, 4933−4941.
(24) De Rosa, C.; Auriemma, F.; Spera, C.; Talarico, G.; Tarallo, O. Comparison between Polymorphic Behaviors of Ziegler−Natta and Metallocene-Made Isotactic Polypropylene: The Role of the Distribution of Defects in the Polymer Chains. *Macromolecules* **2004**, *37*, 1441−1454.
(25) Dai, P. S.; Cebe, P.; Capel, M. Thermal Analysis and X-ray Scattering Study of Metallocene Isotactic Polypropylene Prepared by Partial Melting. *J. Polym. Sci., Part B: Polym. Phys.* **2002**, *40*, 1644−1660.
(26) Wang, Y.; Pan, J. L.; Mao, Y. M.; Li, Z. M.; Li, L. B.; Hsiao, B. S. Spatial Distribution of γ-Crystals in Metallocene-Made Isotactic Polypropylene Crystallized under Combined Thermal and Flow Fields. *J. Phys. Chem. B* **2010**, *114*, 6806−6816.
(27) Zhong, G. J.; Li, Z. M.; Li, L. B.; Mendes, E. Crystalline Morphology of Isotactic Polypropylene (iPP) in Injection Molded Poly(ethylene terephthalate) (PET)/iPP Microfibrillar Blends. *Polymer* **2007**, *48*, 1729−1740.
(28) Somani, R. H.; Hsiao, B. S.; Nogales, A.; Fruitwala, H.; Srinivas, S.; Tsou, A. H. Structure Development during Shear Flow Induced Crystallization of i-PP: In Situ Wide-Angle X-ray Diffraction Study. *Macromolecules* **2001**, *34*, 5902−5909.
(29) Turner, J. A.; Aizlewood, J.; Beckett, D. Crystalline Forms of Isotactic Polypropylene. *Macromol. Chem. Phys.* **1964**, *75*, 134−153.
(30) Zuo, F.; Keum, J. K.; Yang, L.; Somani, R. H.; Hsiao, B. S. Thermal Stability of Shear-Induced Shish-Kebab Precursor Structure from High Molecular Weight Polyethylene Chains. *Macromolecules* **2006**, *39*, 2209−2218.
(31) Wang, Y.; Chen, C.; Xu, J. Z.; Lei, J.; Mao, Y.; Li, Z. M.; Hsiao, B. S. Suppressing of γ-Crystal Formation in Metallocene-Based Isotactic Polypropylene during Isothermal Crystallization under Shear Flow. *J. Phys. Chem. B* **2012**, *116*, 5056−5063.
(32) Nozaki, K.; Endo, Y.; Yamamoto, T.; Naiki, M. Crystallization of α and γ Phases in Isotactic Polypropylene with Low Ethylene Content: Isothermal Crystallization and Secondary Crystallization. *J. Macromol. Sci., Part B* **2003**, *42*, 697−707.
(33) Alamo, R. G.; Kim, M. H.; Galante, M. J.; Isasi, J. R.; Mandelkern, L. Structural and Kinetic Factors Governing the Formation of the γ Polymorph of Isotactic Polypropylene. *Macromolecules* **1999**, *32*, 4050−4064.
(34) Shi, L.; Li, Z. M.; Yang, M. B.; Yin, B.; Zhou, Q. M.; Tian, C. R.; Wang, J. H. Expandable Graphite for Halogen-Free Flame-Retardant of High-Density Rigid Polyurethane Foams. *Polym.-Plast. Technol. Eng.* **2005**, *44*, 1323−1337.
(35) Auriemma, F.; De Rosa, C. Stretching Isotactic Polypropylene: From "cross-β" to Crosshatches, from γ Form to α form. *Macromolecules* **2006**, *39*, 7635−7647.
(36) Dean, D. M.; Register, R. A. Oriented M-Isotactic Polypropylene Crystallized at Atmospheric Pressure. *J. Polym. Sci., Part B: Polym. Phys.* **1998**, *36*, 2821−2827.
(37) Assouline, E.; Fulchiron, R.; Gerard, J. F.; Wachtel, E.; Wagner, H.; Marom, G. γ-Transcrystallization in Isotactic Polypropylene-Based Composites Promoted by Aramid Fibers. *J. Polym. Sci., Part B: Polym. Phys.* **1999**, *37*, 2534−2538.
(38) Cao, Y.; Van Horn, R. M.; Tsai, C. C.; Graham, M. J.; Jeong, K. U.; Wang, B. J.; Auriemma, F.; De Rosa, C.; Lotz, B.; Cheng, S. Z. D. Epitaxially Dominated Crystalline Morphologies of the γ-Phase in Isotactic Polypropylene. *Macromolecules* **2009**, *42*, 4758−4768.
(39) Fujiyama, M.; Wakino, T.; Kawasaki, Y. Structure of Skin Layer in Injection-Molded Polypropylene. *J. Appl. Polym. Sci.* **1988**, *35*, 29−49.
(40) Rule, R.; MacKerron, D.; Mahendrasingam, A.; Martin, C.; Nye, T. Time-Resolved Two-Dimensional Small Angle X-ray Scattering Studies of Oriented Poly(ethylene terephthalate) (PET) Using Paracrystalline Modeling Techniques. *Macromolecules* **1995**, *28*, 8517−8522.
(41) Guinier, A.; Fournet, G. *Small-Angle Scattering of X-rays*; Wiley: New York, 1955.
(42) Zia, Q.; Mileva, D.; Androsch, R. Rigid Amorphous Fraction in Isotactic Polypropylene. *Macromolecules* **2008**, *41*, 8095−8102.
(43) Di Lorenzo, M. L.; Righetti, M. C.; Cocca, M.; Wunderlich, B. Coupling between Crystal Melting and Rigid Amorphous Fraction Mobilization in Poly(ethylene terephthalate). *Macromolecules* **2010**, *43*, 7689−7694.
(44) Righetti, M. C.; Di Lorenzo, M. L.; Tombari, E.; Angiuli, M. The low-Temperature Endotherm in Poly(ethylene terephthalate): Partial Melting and Rigid Amorphous Fraction Mobilization. *J. Phys. Chem. B* **2008**, *112*, 4233−4241.
(45) Xu, H.; Cebe, P. Heat Capacity Study of Isotactic Polystyrene: Dual Reversible Crystal Melting and Relaxation of Rigid Amorphous Fraction. *Macromolecules* **2004**, *37*, 2797−2806.
(46) Bai, H. W.; Luo, F.; Zhou, T. N.; Deng, H.; Wang, K.; Fu, Q. New Insight on the Annealing Induced Microstructural Changes and Their Roles in the Toughening of β-Form Polypropylene. *Polymer* **2011**, *52*, 2351−2360.